Accepted for publication in ***Computers & Fluids***, February 2014

Counter-gradient diffusion in a slot-ventilated enclosure assessed by LES and RANS

T. van Hooff * [(a,b)], B. Blocken [(a,b)], P. Gousseau [(a)], G.J.F. van Heijst [(c)]

(a) Building Physics and Services, Eindhoven University of Technology, Eindhoven, the Netherlands

(b) Building Physics Section, Department of Civil Engineering, Katholieke Universiteit Leuven, Leuven, Belgium

(c) *Fluid Dynamics Laboratory, Eindhoven University of Technology, Eindhoven, the Netherlands*

Abstract:

In Computational Fluid Dynamics (CFD) studies for the prediction of room airflow the Reynolds-averaged Navier-Stokes (RANS) approach is often used, in which only the averaged quantities are computed, whereas the effect of turbulence is modeled. Since the RANS approach does not provide information on the velocity and concentration fluctuations, turbulent mass transport is often modeled using the standard gradient-diffusion hypothesis, which relates the turbulent mass flux to the mean concentration derivatives. This paper presents a CFD analysis of pollutant dispersion in an enclosure ventilated by a transitional wall jet (Re ≈ 2,500), using validated high-resolution RANS and Large Eddy Simulations (LES). The LES simulations show that a counter-gradient turbulent mass flux is present, indicating that the standard gradient-diffusion hypothesis used in RANS is not valid in the entire flow domain. However, it is shown that for this particular case, the convective mass fluxes dominate over the turbulent mass fluxes, and that the predicted pollutant concentrations by RANS will therefore not differ significantly from the results obtained with LES.

Keywords: Computational Fluid Dynamics (CFD); dispersion modeling; eddy-diffusivity concept; mechanical ventilation; reduced-scale setup.

* Corresponding author:
Twan van Hooff
Building Physics and Services, Eindhoven University of Technology
P.O. Box 513, 5600 MB Eindhoven, the Netherlands.
Tel.: +31 (0)40 247 5877,
Fax +31 (0)40 243 8595
E-mail address: t.a.j.v.hooff@tue.nl

1. Introduction

The numerical modeling of room airflow started in the nineteen-seventies, when Nielsen performed Reynolds-averaged Navier-Stokes (RANS) simulations for a mixing ventilation case with and without buoyancy effects [1-3]. Since those early simulations, a lot of research efforts have focused on the numerical modeling of room airflow. Among others, Awbi [4], Jones and Whittle [5], Kato et al. [6], Gan and Awbi [7], Murakami et al. [8], Chen [9-11], Nielsen [12,13], Moureh and Flick [14,15], Sørensen and Nielsen [16], van Hooff and Blocken [17,18], Li and Nielsen [19], van Hooff et al. [20], Rundle et al. [21], Ramponi and Blocken [22] and Cao and Meyers [23] published papers on the numerical modeling of room airflow. The simulations have become more complex over time, as a result of more complex room geometries, the inclusion of pollutant dispersion modeling and the use of more sophisticated numerical approaches such as Large Eddy Simulation (LES). However, nowadays, steady RANS simulation with a turbulence model to provide closure is still the most often used approach, although there are several challenges associated with RANS turbulence models. Van Hooff et al. [20] mentioned three specific challenges in room airflow modeling, namely the modeling of turbulence anisotropy, transitional flow (low Reynolds numbers) and adverse pressure gradients. In their study, 3D steady RANS simulations of room airflow at slot Reynolds numbers of 1000-2500 were compared with PIV measurements in a reduced-scale water filled model, indicating that, despite the complexity of the studied flow problem, the low-Reynolds number k-ε model (LR k-ε) by Chang et al. [24], the SST k-ω model by Menter [25] and the low-Re stress-omega Reynolds Stress Model (RSM) [26], based on the omega equations and the Launder-Reece-Rodi (LRR) model by Launder et al. [27], provided a fair (SST k-ω, RSM) to good (LR k-ε) agreement for the mean velocity field.

Another important consideration in room airflow research is pollutant dispersion. In turbulent flows, dispersion is the result of the combination of molecular diffusion, convection and turbulent diffusion, where the first is often negligibly small compared with the two others. In general, since steady RANS simulations do not explicitly provide the velocity and concentration fluctuations, steady RANS simulations of dispersion use the standard gradient-diffusion hypothesis (the adjective "standard" will be omitted in the remainder of the paper) which relates the turbulent mass flux to the mean mass concentration gradient using the turbulent (or eddy) mass diffusivity D_t. The value of D_t is deduced from the computed turbulent viscosity ν_t and the input value of the turbulent Schmidt number Sc_t ($D_t = \nu_t/Sc_t$). In general, a value for Sc_t between 0.5 and 0.9 is used. In the commercial CFD code Fluent 6.3 for example, the default value is 0.7 [28]. The Sc_t value is in general lower than unity due to the higher efficiency of scalar transport compared to momentum transport. The lower efficiency of turbulent momentum transport is due to the presence of a pressure gradient term in the momentum equations which suppresses turbulent transport and which is not present for scalar transport [29]. Several publications have focused on determining the Sc_t value that provides the most accurate results. He et al. [30] studied the adequacy and accuracy of using a constant Sc_t for predicting pollutant dispersion in jet-in-cross flows and found that a value of 0.2 resulted in the best agreement with the measurements. Lubbers et al. [29] used Direct Numerical Simulation (DNS) to determine Sc_t for passive scalar mixing in a free turbulent round jet and found an average value of $Sc_t = 0.74$ for this particular case, which resembles the values obtained from experiments by Chevray and Tutu [31]. Yimer et al. [32] studied an axisymmetric turbulent free jet, for which they empirically determined Sc_t based on previous mean velocity and passive scalar measurements. They concluded that Sc_t increased from 0.62 on the jet axis to 0.82 in the region where the intermittency factor δ is still 1. An intermittency factor $\delta = 1$ indicates a fully turbulent jet region. The average Sc_t value for the region with $\delta = 1$ amounts to 0.69, which is close to the recommended values of $Sc_t = 0.7$ for species transport in jets by Spalding [33] and of $Sc_t = 0.72$ by Hinze [34]. Yimer et al. [32] concluded that

there is no physical reason to use much lower values for Sc_t in these cases. Awbi [35] reports values found by Rodi [36], who recommended $Sc_t = 0.9$ for near wall flows (boundary layer or wall jets), $Sc_t = 0.5$ for plane jets and mixing layers and $Sc_t = 0.7$ for axisymmetric jets. Finally, Tominaga and Stathopoulos [37] studied the effect of the turbulent Schmidt number on pollutant dispersion and found that the results were highly dependent on the turbulent Schmidt number. The optimum values for Sc_t were shown to be widely distributed (0.2–1.3).

Although several studies have focused on the value of Sc_t, to the knowledge of the authors, no room airflow studies have been published in which the validity of the gradient-diffusion hypothesis is investigated. In other research areas there are not much similar studies either. Tominaga and Stathopoulos [37] provided some information about convective and diffusive fluxes for the case of dispersion around a building in an atmospheric boundary layer flow, but they only considered a few locations on the roof. Gousseau et al. [38,39] assessed the validity of the gradient-diffusion hypothesis for pollutant dispersion around isolated buildings by comparing high-resolution LES results with RANS results. The study showed that a counter-gradient mechanism governs turbulent mass transfer in the streamwise direction. This indicates that the commonly used gradient-diffusion hypothesis in RANS is invalid for this particular case. However, the erroneous prediction of the streamwise turbulent mass flux by the RANS models did not significantly influence the results since convection was shown to act as the dominant mechanism of mass transport in this direction. It should be noted that in other cases, the invalidity of the gradient-diffusion hypothesis might lead to larger errors in the predicted pollutant concentration field; further studies are therefore needed on this topic to address the possible errors for a range of flow problems (e.g. room airflow, urban wind flow).

In this paper, a detailed analysis of the transport process of a passive gaseous pollutant in a room ventilated by a transitional plane wall jet is presented. The relative influence of convective and turbulent fluxes in the mass transport process is analyzed after which their role in the prediction accuracy of RANS and LES simulations of the concentration field is clarified. First, the room geometry is described in Section 2. Section 3 outlines the experimental setup that has been used to obtain validation data for the numerical simulations. The governing equations are addressed in Section 4. Section 5 presents the CFD model. In Section 6, the validation study is outlined, followed by the results of the pollutant dispersion simulations. Finally, sections 7 (discussion) and 8 (conclusions) conclude the paper.

2. Room geometry

The room under study is a reduced-scale cubical enclosure (L^3) with edges L = 0.3 m. It has a linear ventilation inlet at the top with a height of h/L = 0.1 and a width of w/L = 1, and a linear ventilation outlet at the bottom of the opposing wall (h/L = 0.0167) (see Fig. 1a). The walls have a thickness d (d/L = 8/30). The chosen configuration represents a mixing ventilation case; the ventilation air enters the enclosure through the inlet in the upper part of the room (wall jet), it mixes with the room air, and the diluted air is exhausted through the outlet (e.g. [35]). This geometrical configuration is one of the most often studied configurations in ventilation research, and was used, among others, by Nielsen [2,40] and Chen [9,10].

An important parameter for indoor airflow studies is the slot Reynolds number, which is defined based on the inlet height as $Re = U_0 h/\nu$, with U_0 the bulk inlet velocity and ν the kinematic viscosity at room temperature (≈ 20°C) (see Fig. 1b). For this study a Re-value of 2,500 was used, which was shown to result in a transitional flow pattern, including pronounced Kelvin-Helmholtz-type instabilities in the outer region of the wall jet (shear layer) [41].

3. Reduced-scale experiments

Particle Image Velocimetry (PIV) measurements were performed in the test section of a reduced-scale water-filled model to provide validation data [41,42]. The reduced-scale model consists of a water column, a conditioning section and a cubic test section of 0.3 x 0.3 x 0.3 m^3 (Fig. 2). More information on the experimental setup can be found in van Hooff et al. [42].

A 2D PIV system was used to conduct the measurements. It consisted of a Nd:Yag (532 nm) double-cavity laser (2 x 200 mJ, repetition rate < 10 Hz) used to illuminate the field of view, and one CCD (Charge Coupled Device) camera (1376 x 1040 pixel resolution, 10 frames/s) for image acquisition. The laser was mounted on a translation stage and was positioned above the cubic test section to create a laser sheet in the vertical center plane of the cube (z/L = 0.5); the camera was positioned perpendicular to the water cube. Seeding of the water was provided by hollow glass micro spheres (3M; type K1) with diameters in the range of 30 – 115 μm.

Two sets of PIV measurements were performed. The first set focused on the entire cross-section of the cube, i.e. a target area of 0.3 x 0.3 m^2 (= ROI1) (Fig. 3a). The second set focused on a smaller target area of 0.18 x 0.12 m^2 (W x H) in the proximity of the inlet, enabling a higher measurement resolution (= ROI2) (see Fig. 3a). The required measuring frequency was estimated from the integral length scale (= inlet height) and the characteristic velocity (i.e. inlet velocity) and was set 2 Hz. Each measurement set consists of 360 uncorrelated samples (i.e. averaging time = 180 seconds). The errors associated with PIV measurements can be divided in systematic and repeatability errors. The systematic errors are present for each sample and consist of a range of errors that are associated with the PIV measurement technique and methodology [43]. To minimize the systematic errors the best practice guidelines of Keane and Adrian [44] and Prasad [43] have been taken into account. The repeatability, or random, error is a statistical error. The uncertainty associated with the repeatability error can be assessed using the central limit theorem (e.g. [45]). The uncertainty of the measurement results is around 2-4% in the largest part of the test section and is slightly higher in the shear layer and boundary layer areas as a result of the locally higher turbulence levels [41]. For the validation study in this paper the time-averaged velocities at three vertical lines inside the enclosure are used (Fig. 3b). Note that the results for y/L < 0.05 are not used because they are less accurate due to reflections of the laser sheet on the glass bottom of the cube. For more measurement results for this specific room geometry with h/L = 0.1 and Re ≈ 2,500, the reader is referred to van Hooff et al. [41]. The measurement results will be presented together with the CFD simulation results in Section 6.

4. RANS, LES and dispersion modeling

4.1. RANS and turbulence models

In the RANS approach, the Reynolds decomposition splits the flow variables into an average and a fluctuating part. Only the averaged quantities are resolved and the effect of turbulence on the average flow field (Reynolds stresses) is modeled with turbulence models. In this study, two turbulence models will be used and compared: the LR k-ε model by Chang et al. [24], and the RSM model as described by Wilcox [26]. The LR k-ε model is a linear two-equation eddy-viscosity model that uses the Boussinesq hypothesis which relates the Reynolds stresses to the mean velocity gradients by using an eddy (or turbulent) viscosity μ_t. The RSM model is a second-order closure model in which additional transport equations are solved for each of the Reynolds stresses. Using a second-order closure model, e.g. RSM, one can more accurately take into account the effect of the Reynolds stresses on the flow field, which should provide superior results for these flows (e.g. [8,46,47]).

4.2. LES and subgrid-scale models

In LES, a spatial-filtering operator is applied to the Navier-Stokes equations, which separates the large scales of motion, which are explicitly resolved, from the small scales, which have a more universal behavior and can therefore be modeled. A subgrid-scale (SGS) model is used to model the effect of the small scales on the resolved flow field. For the LES simulations in this paper, the dynamic Smagorinsky SGS model is used [48-50]. The application of LES is especially relevant in studies of mass transport, since this process is mainly governed by the largest scales of motion.

4.3. Dispersion modeling

The instantaneous pollutant concentration c (kg m^{-3}) is treated as a scalar transported by an advection-diffusion equation (Eulerian approach):

$$\frac{\partial c}{\partial t} + \vec{u}.\nabla c = -\nabla.\overrightarrow{q_m} + s_c \tag{1}$$

where $\overrightarrow{u}$ is the velocity vector, s_c a source term and $\overrightarrow{q_m}$ the mass flux due to molecular diffusion. Applying the Reynolds decomposition to the variables (x = X + x' where X = <x> and x' are the mean and fluctuating components of x, respectively) and averaging Eq. (1) yields:

$$\nabla.\left(\overrightarrow{Q_m} + \overrightarrow{Q_c} + \overrightarrow{Q_t}\right) = S_c \tag{2}$$

In this equation, $\overrightarrow{Q_m}$ is the mean molecular mass flux (kg $m^{-2}s^{-1}$), which is proportional to the gradient of mean concentration (Fick's law):

$$Q_{m,i} = -D_m \frac{\partial C}{\partial x_i} \tag{3}$$

where D_m is the molecular mass diffusivity ($m^2\ s^{-1}$), and i indicates the coordinate (x_1, x_2, x_3 = x, y, z). In general, the molecular mass flux is negligible in comparison with the mean convective and turbulent fluxes, symbolized by $\overrightarrow{Q_c}$ and $\overrightarrow{Q_t}$, respectively. Note that the adjective "mean" will be omitted in the remainder of the paper. The convective mass flux is given by:

$$Q_{c,i} = U_i C \tag{4}$$

And the turbulent mass flux is defined as:

$$Q_{t,i} = < u_i' c' > \tag{5}$$

However, the steady RANS approach does not provide the velocity and concentration fluctuations. Therefore, the turbulent mass flux must be computed based on the mean variables. In general, the gradient-diffusion hypothesis is adopted, by analogy with molecular diffusion:

$$Q_{t,i:RANS} = -D_t \frac{\partial C}{\partial x_i} \tag{6}$$

where D_t is the turbulent mass diffusivity. The value of D_t is deduced from the computed turbulent viscosity ν_t and the input value of the turbulent Schmidt number $Sc_t = \nu_t/D_t$. As stated in the introduction, the value of Sc_t used in previous studies differs significantly. A recommended value for dispersion in jets is 0.7 [29,32-34]. Note that this hypothesis does not represent the true physical process of turbulent mass diffusion; it merely relates turbulent mass diffusion to the concentration gradient using the turbulent mass diffusivity since velocity and concentration fluctuations are not available in RANS simulations.

In LES, the total turbulent mass flux Q_t is the sum of the flux due to the resolved turbulent fluctuations and the SGS mass flux:

$$Q_{t,i;\,LES} = < \overline{u}_i' \overline{c}' > + < q_{SGS,i} > \tag{7}$$

The instantaneous SGS mass flux $\overrightarrow{q_{SGS}}$ is assumed proportional to the gradient of resolved concentration:

$$q_{SGS,i} = \overline{u_i c} - \overline{u}_i \overline{c} = -D_{SGS} \frac{\partial \overline{c}}{\partial x_i} \tag{8}$$

where the overbar denotes the filtering operation and D_{SGS} is the SGS mass diffusivity. In this study, D_{SGS} is computed via the SGS viscosity ν_{SGS} and the SGS Schmidt number $Sc_{SGS} = \nu_{SGS}/D_{SGS}$. Here, Sc_{SGS} is computed dynamically, with a similar procedure as the Smagorinsky coefficient C_s [51]. Note that the turbulent mass flux in LES simulations is directly obtained from the resolved turbulent fluctuations (u′ and c′; see Eq. 7), which requires no additional modelling efforts or assumptions as long as the contribution of the SGS mass flux to the total turbulent mass flux is very small. In the remainder of the paper all mean concentrations will be expressed in non-dimensional form as a concentration coefficient K:

$$K = \frac{C}{C_{ref}} \tag{9}$$

where the reference concentration C_{ref} is defined as:

$$C_{ref} = \frac{S_c V}{h_{inlet}^{\,2} U_0} \tag{10}$$

with S_c the pollutant source rate (kg m^{-3}s^{-1}), V the enclosure volume (m^3), h_{inlet} the inlet height (m) and U_0 the inlet velocity (m s^{-1}). In addition, a reference flux magnitude Q_0 (kg m^{-2}s^{-1}) will be used to

make the convective and turbulent mass fluxes non-dimensional. The reference flux magnitude Q_0 can be calculated from the inlet velocity and from the reference concentration C_{ref} (kg m^{-3}) as $Q_0 = C_{ref}U_0$.

5. CFD simulations: computational settings and parameters

5.1. Computational geometry and grid

The computational model is a replica of a part of the experimental setup as described in Section 3 and as previously presented in van Hooff et al. [20]. Note that the simulations are also performed for the reduced-scale model, filled with water (ρ = 998.2 kg m^{-3} at 20°C). Only a small part of the conditioning section, i.e. the contraction upstream of the test section, is included in the model (Fig. 4a). Note that the outlet is extended in the x-direction to enhance convergence of the simulations.

The computational grid was created using the surface-grid extrusion technique presented in van Hooff and Blocken [17]. A grid with 1,386,400 cells was used for both the steady RANS and the LES simulations. The grid size was based on a previous grid-sensitivity analysis, which indicated nearly grid-independent results [20]. The number of cells over the inlet height and outlet height is 50 and 20, respectively (Fig. 4c,d). The dimensionless wall distances y^* at the top surface (y/L = 1) in the center plane (z/L = 0.5) are between 0.12 and 0.68. The low values for y^* enable the use of low-Reynolds number modeling (LRNM) for the RANS models, which implies solving the flow all the way down to the wall, including the thin viscous sublayer. The grid resolution for the application of LRNM should be very high, preferably with y^* values lower than 1. The numerical accuracy using LRNM is larger than when using wall functions, in which semi-empirical formulae are used to bridge the region between the wall and the center of the wall-adjacent cell. Also for LES the y^* value should preferably be about 1 or smaller.

5.2. Boundary conditions

The boundary conditions for the CFD simulations were chosen to replicate those of the PIV experiments as closely as possible. A uniform velocity was imposed at the CFD inlet (see Fig. 4a), which was based on the Reynolds number at the actual ventilation inlet during the experiments and the ratio between the height of the CFD inlet (h/L = 0.3) and the actual ventilation inlet (h/L = 0.1); $U_{inlet;CFD}$ = 0.025 m s^{-1} for Re ≈ 2,500 (see Fig. 4a). As a result of the contraction between the CFD inlet and the actual ventilation inlet, the velocity at the actual ventilation inlet is approximately three times higher than the one imposed at the CFD inlet. The turbulence parameters were specified based on the hydraulic diameter and the turbulence intensity. The hydraulic diameter D_h was calculated using $D_h = (4WH)/(2(W+H))$, with H the height and W the width of the CFD inlet (Fig. 4a). The measured turbulence intensity (u_{RMS}/U_M) in the wall jet region at x/L = 0.2 was around 3-4% [41]. U_M is the maximum local velocity and it will also be used in the remainder of the study to make the velocities non-dimensional (U/U_M) (Fig. 1b). Note that U_M is defined as the local maximum time-averaged x-velocity, and thus varies with both x/L and Re. A constant turbulence intensity of 18% was imposed at the CFD inlet, based on the inlet velocity at the CFD inlet (= 0.025 m/s). Note that the turbulence intensity at the CFD inlet is higher since the contraction will reduce the turbulence intensity to the measured values. As a result of the contraction the resulting turbulence intensity and turbulent kinetic energy values just after the entrance of the cubic test section correspond with the measured values (see Figure 6b-c). For the LES computations, a time-dependent inlet profile is generated by using the vortex method [52] with a number of vortices N_v = 190. As shown by Sergent [53], the influence of

small changes to the number of vortices on the generated velocity fluctuations is negligibly small. Zero static pressure was imposed at the outlet and the surfaces were modeled as smooth no-slip walls.

To incorporate pollutants, a constant and uniform pollutant source term $S_c = 0.02$ kg $m^{-3}s^{-1}$ was imposed in the whole cubic enclosure. The pollutant is passive and has the same density as the ambient fluid (= water: 998.2 kg m^{-3}), implying absence of buoyancy effects. The concentration at the ventilation inlet equals zero, which corresponds to the supply of fresh water.

5.3. Solver settings

The simulations were performed with the Fluent 6.3.26 CFD code. For the RANS simulations, pressure-velocity coupling was taken care of by the SIMPLEC algorithm, pressure interpolation is second order and second-order upwind discretization schemes are used for all transport equations (momentum, turbulence and concentration). Convergence was monitored carefully. For the majority of the simulations oscillatory convergence was present. As discussed in Ramponi and Blocken [22] and van Hooff et al. [20,53], steady RANS CFD simulations can exhibit oscillatory convergence, resulting in fluctuating values of the studied parameters as function of the number of iterations. Solely looking at the residuals for judging convergence is therefore not enough and might even be misleading. To obtain an "average" solution, the results of the RANS simulations were averaged over a sufficiently large number of iterations. In this case, the averaging took place over an interval of 4,000 or an interval of 20,000 iterations, depending on the Re-value, grid size and the turbulence model. More information on the oscillatory convergence observed in the CFD simulations for this mixing ventilation study can be found in van Hooff et al. [20]. The dispersion simulations using RANS were conducted in two steps. First, the steady flow field was obtained. Second, the transport equation for concentration was solved to obtain the spatial distribution of the pollutant.

For the LES simulations, the filtered momentum equation was discretized with a bounded central-differencing scheme. A second-order upwind scheme was used for the concentration equation. Pressure interpolation was second order. Time integration is second-order implicit. Pressure-velocity coupling was taken care of by the PISO algorithm. The results of the LES computation presented here were averaged over 200,000 time steps, which corresponds to 800 s, which is 20 times the approximated value of t^*. The parameter t^* is the time needed for the jet to make one circulation in the test section, and is defined as $t^* = (4L)/U_{average}$, with $U_{average}$ the average velocity of the jet around the recirculation cell. The time step Δt was based on a maximum CFL number of 1 and is equal to $\Delta t = 0.004$ s. It was verified that the averaging time is sufficient to obtain statistically-steady results by monitoring the evolution of K with time (moving average).

6. CFD simulations: results

6.1. Mean velocity profiles

Figure 5 compares the measured and simulated profiles of the time-averaged dimensionless x-velocity (U/U_M) along three vertical lines in the test section center plane, at $x/L = 0.2$, $x/L = 0.5$ and $x/L = 0.8$ (Fig. 3b). Note that the experimentally obtained velocity profile in Figure 5a does not resemble a clear top-hat profile, which is the result of the lower measurement resolution in ROI1 [42]. A comparison between the measured and simulated profiles of mean x-velocity in ROI2 is provided in Figure 6, where the experimental top-hat profile is clearly present. Figure 5a shows that at $x/L = 0.2$ the simulations with the LR k-ε, RSM model and LES model provide fairly identical results, which are

in relatively close agreement with the measurements. Also at x/L = 0.5 (Fig. 5b), the two RANS turbulence models and LES provide roughly the same velocity profiles, which resemble the measured velocity profile to a large extent. Figure 5c shows the velocity profiles at x/L = 0.8, at which the largest differences between the two RANS results and the LES results can be observed. The RSM model predicts $U/U_M = 1$ to be located at y/L = 0.74, which is much lower than the measured location. The location of maximum jet velocity predicted by the LR k-ε model (y/L = 0.82) is also too low at x/L = 0.8, however, these results are in much closer agreement with the measurements. The LES model clearly outperforms the RANS models at x/L = 0.8; the numerical prediction of the vertical location of the maximum jet velocity is almost identical to the measured location.

Figure 6 shows the results of mean x-velocity at x/L = 0.2 obtained from the PIV measurements in a smaller ROI with a higher spatial resolution (Fig. 3a: ROI2), which are compared with the results of the RANS simulations and of the LES simulation. The velocity profiles in the wall jet predicted by the LES model are quite similar to the ones predicted by the LR k-ε and the RSM model, and the results of all three models show a good agreement with the measurement results at this specific location (x/L = 0.2).

In summary, it can be concluded that the LR k-ε model provides fairly accurate predictions of the mean velocity profiles, although it has some difficulties with the prediction of the jet detachment and the resulting location of maximum jet velocity at x/L = 0.8. The results obtained with the RSM model are less accurate, especially at x/L = 0.5 and x/L = 0.8. The LES model provides good to very good predictions of the velocity field at all three locations (on average within 5%).

6.2. Turbulent kinetic energy profiles

Since the 2D PIV measurements only provided the velocity components in the streamwise (U, u_{RMS}) and vertical direction (V, v_{RMS}), the RMS value in the lateral direction (w_{RMS}) is unknown. To be able to calculate the turbulent kinetic energy, the correlation between the normal stresses in a 2D wall jet, as described by Nielsen [55], is used:

$$w_{RMS} \approx \sqrt{0.8}\, u_{RMS} \tag{11}$$

The turbulent kinetic energy can subsequently be calculated using:

$$\mathrm{k} = \frac{1}{2}\left({u_{RMS}}^2 + {v_{RMS}}^2 + {w_{RMS}}^2 \right) \tag{12}$$

The profiles of turbulent kinetic energy are shown in Figure 6b (x/L = 0.2) and Figure 6c (x/L = 0.5). It is shown that at x/L = 0.2, the LR k-ε model, RSM model and the LES model overpredict the turbulent kinetic energy in the core region (0.94 < y/L 0.97) of the wall jet. In the outer region of the wall jet (shear layer: y/L ≈ 0.9), the RSM model underpredicts the turbulent kinetic energy, and the LR k-ε model and LES model overpredict the turbulent kinetic energy. Below the wall jet, i.e. y/L < 0.85, the best agreement is obtained with the RSM model. Figure 6c indicates that the numerical results obtained with the LR k-ε and RSM model at x/L = 0.5 show a fair to good agreement with the measurement results in the boundary layer region (0.97 < y/L < 1.0), whereas the LES model overpredicts the value of turbulent kinetic energy. In the shear layer (0.85 < y/L < 0.91) the values are again slightly overpredicted by the LR k-ε model and the LES model, and underpredicted by the RMS model. Below the wall jet region (y/L < 0.82), the best agreement is obtained with the RSM model, followed by the LES model. 6.3. Velocity vector fields

Figure 7 shows the experimentally and numerically obtained velocity vector fields in the vertical center plane of the cube, with an indication of the location of jet detachment (x_{det}/L) and the center of the recirculation cell (● (x/L; y/L)). The value of x_{det}/L obtained with the LES simulation shows the best agreement with the experimentally obtained value; both are $x_{det}/L \approx 0.75$. The results obtained with the RSM model show the largest deviation with a too early detachment of the wall jet: $x_{det}/L \approx 0.6$ (Fig. 7c). The location of the center of the recirculation cell (●) is also most accurately predicted by LES. The coordinates obtained by the PIV measurements (Fig. 7a: ● = (0.47; 0.41)), closely resemble the coordinates obtained by the LES simulation (Fig. 7d: ● = (0.47; 0.43)). The LR k-ε model predicts coordinates (Fig. 7b: ● = (0.44; 0.43)) that show a fair agreement with the measured ones. The center of the recirculation cell predicted by the RSM model again shows the largest deviation (Fig. 7c: ● = (0.40; 0.34)). These vector fields confirm the ability of the LES model to accurately predict the flow pattern inside the enclosure. Furthermore, the LR k-ε model fairly accurately predicts the flow pattern, whereas the results obtained with the RSM model show relatively large deviations.

6.4. Pollutant dispersion

6.4.1. Influence of turbulent Schmidt number

To test the influence of the turbulent Schmidt number for the case under study, simulations with the LR k-ε model, as this model performs better than the RSM model, have been performed with $Sc_t = 0.3$, 0.7 and 1.0. Vertical profiles of the calculated dimensionless concentrations K in the vertical center plane of the enclosure are depicted in Figure 8, together with those obtained with LES. It can be seen that the results obtained with LES show a close agreement with the results obtained with $Sc_t = 0.7$. This observation can be made at all three locations and seems to justify using the Fluent default value of $Sc_t = 0.7$, at least for this particular case. Furthermore, Figure 8 shows that the differences in K obtained with different Sc_t values are relatively small. The deviations between the results with $Sc_t = 0.3$ and with $Sc_t = 0.7$ are below 25%. The differences between the results obtained with $Sc_t = 0.7$ and with $Sc_t = 1.0$ are within 12%.

6.4.2. Analysis of mass fluxes

In LES studies on pollutant dispersion in the urban environment the contribution of the non-resolved scales to the turbulent flux was often neglected in the total mass flux (e.g. [38,55]). Figure 9 shows the ratio of the magnitudes of $\overrightarrow{Q_{SGS}}$ and $\overrightarrow{Q_t}$ ($\left|\overrightarrow{Q_{SGS}}/\overrightarrow{Q_t}\right|$) in the vertical center plane (z/L = 0.5), in which $Q_{SGS,i} = \langle q_{SGS,i} \rangle$ in Eq. (7). It can be seen that the ratio is smaller than 5.0E-02 in the largest part of the flow domain, which indicates that the magnitude of the subgrid-scale fluxes is relatively small compared to the turbulent fluxes. An exception is present just below the wall jet, where the ratio is between 1.0E-01 and 5.0E-02, however, this still indicates that the SGS fluxes are 10-20 times smaller than the turbulent fluxes. In general, Figure 9 shows that with the currently applied grid resolution and SGS modeling the magnitude of $\overrightarrow{Q_{SGS}}$ is at least 20 times smaller than that of $\overrightarrow{Q_t}$ in the largest part of the domain. Although the ratio of $\left|\overrightarrow{Q_{SGS}}/\overrightarrow{Q_t}\right|$ is small, the SGS contribution is included in the definition of the turbulent mass flux in this and in consecutive figures in accordance to Eq. (7).

Figure 10 shows the non-dimensional convective mass fluxes ($Q_{c,i}/Q_0$) in the streamwise (Fig. 10a,c,e) and the vertical direction (Fig. 10b,d,f) obtained from the two steady RANS simulations and

the LES simulation (time-averaged). It can be seen that the contours obtained with the LR k-ε model are quite similar to the contours obtained with the unsteady LES simulation. Only small differences in the shape of the contours are visible, and the values of the non-dimensional convective fluxes are also quite similar. The results obtained with the RSM model show larger deviations, especially concerning the shape of the contours. In addition to the contours of the non-dimensional convective mass fluxes, the isolines for K = 0.04; 0.12; 0.20; 0.28 and 0.34 are plotted in Figure 10. These isolines show that the maximum values of the concentration K obtained with the RSM model are higher than those obtained with the LR k-ε and the LES model.

The non-dimensional turbulent mass fluxes ($Q_{t,i}/Q_0$) are depicted in Figure 11a-d. The turbulent mass fluxes from the LES simulation are calculated using Eq. (7). For the steady RANS simulations the turbulent fluxes are obtained using the gradient-diffusion hypothesis (Eq. (6)). The first general observation to be made is that the turbulent fluxes depicted in Figure 11 are considerably smaller than the convective fluxes in Figure 10. The absolute values of the turbulent fluxes $|Q_{t,i}/Q_0|$ are in general one order of magnitude smaller than those of the convective fluxes, both for the results obtained by the RANS simulations, and those by the LES simulation. Furthermore, it can be seen that the turbulent fluxes obtained with the RSM model deviate from those obtained with the LR k-ε model. The values for $Q_{t,x}$ on the right side of the cube are for example one order of magnitude smaller for the RSM model (Fig. 11c) than for the LR k-ε model (Fig. 11a). The circles with a '+' or '-' sign indicate whether there is a positive or negative concentration derivative in the corresponding direction, respectively. Fig. 11a-d show that the turbulent fluxes are positive in regions with negative concentration derivatives ($\partial C/\partial x < 0$; $\partial C/\partial y < 0$), and vice versa, which is the result of the gradient-diffusion hypothesis as shown in Eq. (6).

Figure 11e,f shows the turbulent fluxes in the vertical center plane obtained from the LES simulation. In addition to contours of $Q_{t,i}/Q_0$, the isoline $\partial C/\partial x = 0$ is depicted, as well as the areas with positive or negative concentration derivatives, indicated with a '+' or '-' sign, respectively. The contours of $Q_{t,i}/Q_0$ by LES differ significantly from those obtained from the RANS simulations. Figure 11e shows that in the outer region of the wall jet there is a negative concentration gradient ($\partial C/\partial x < 0$) in the x-direction, while there is also a negative turbulent flux ($Q_{t,x}/Q_0 < 0$) in this region. This observation shows that the gradient-diffusion hypothesis is not valid in this region; a counter-gradient mass transport mechanism is present characterized by $Q_{t,i}$ and $\partial C/\partial x_i$ being of the same sign. The same holds for the region in the bottom left corner of the cube; in this area a positive value of ($\partial C/\partial x > 0$) exists in combination with a positive turbulent mass flux ($Q_{t,x}/Q_0 > 0$). Figure 11f shows the turbulent fluxes in the vertical direction obtained with LES. There is a region with $\partial C/\partial y < 0$ below the wall jet in combination with a negative turbulent mass flux ($Q_{t,y}/Q_0 < 0$). In the vicinity of the outlet a positive turbulent mass flux ($Q_{t,y}/Q_0 > 0$) is present in an area with $\partial C/\partial y > 0$. The four observations described above indicate the fact that the gradient-diffusion hypothesis is not valid in the entire flow domain. The inability of the gradient-diffusion hypothesis to accurately predict the turbulent fluxes can be attributed to the effects of coherent structures inside the flow domain, which was also indicated by Gousseau et al. [40] for dispersion around an isolated building. These coherent structures drive the counter-gradient transport in the enclosure.

Figure 12 shows the ratio of turbulent to convective mass flux components ($|Q_{t,i}/Q_{c,i}|$) for both the streamwise (Fig. 12a) and the vertical direction (Fig. 12b). It can be seen that the turbulent mass flux is in general one or even two orders of magnitude smaller than the convective mass flux, both in the streamwise and the vertical direction. There are some regions, for example in the vicinity of the downstream wall and the exhaust (Fig. 12a), and in the outer region of the wall jet (Fig. 12b), where the turbulent flux is about equal to the convective flux ($|Q_{t,i}/Q_{c,i}| = 1$) and where the turbulent transport thus plays a significant role. However, for this particular case, in the largest part of the enclosure, the turbulent flux plays a less important role in the pollutant dispersion process than the convective flux .

This implies that, although the gradient-diffusion hypothesis is partly violated for the case under study, this does not necessarily have a large impact on the accuracy of the computed pollution concentration. This statement is indeed supported by Figure 13, which shows the distribution of the dimensionless concentration K in the vertical center plane (z/L = 0.5) obtained with the steady RANS simulations and with LES. Although there are differences in the distribution of K, the general concentration distribution, as well as the absolute values, obtained by steady RANS with the LR k-ε model do not differ significantly from the concentrations obtained with LES. Figure 8 shows differences between the LES model and steady RANS with the LR k-ε model ($Sc_t = 0.7$) that are generally below 10%. However, Figure 13 shows that local differences between the LES model and steady RANS with the LR k-ε model ($Sc_t = 0.7$) can go up to a factor 2. The distribution of K obtained with the RSM model shows larger deviations from the LES results.

7. Discussion

In the preceding sections we have presented an analysis of the validity of the standard gradient-diffusion hypothesis for indoor dispersion modeling in a slot-ventilated enclosure. Although the gradient-diffusion hypothesis is not always valid due to the presence of counter-gradient transport mechanisms, it has been shown that for the case under study the turbulent fluxes are one or even two orders of magnitude smaller than the convective fluxes in the largest part of the enclosure. This indicates the strong importance of convection in this particular case and underlines the importance of primarily predicting the mean flow field in an accurate way. As a result, the choice of the value of the turbulent Schmidt number has a rather limited influence, at least for the particular case under study.

The studied configuration is a simplified version of an actual room. Future work will focus on additional room geometries and flow configurations, including different slot Reynolds numbers, and including thermal effects and internal objects. The use of different formulations for the turbulent scalar flux in RANS simulations can be considered. In addition to the standard gradient-diffusion hypothesis, the performance of the generalized gradient-diffusion hypothesis [56] and the high-order gradient-diffusion hypothesis can be studied [57]. Future work will also consist of validating both airflow and pollutant concentrations in the enclosure. Measurements of turbulent mass fluxes can for example be performed using Particle Tracking Velocimetry (PTV) in combination with PIV. The use of PTV would enable an experimental validation of the turbulent mass flux vector and the gradient-diffusion hypothesis, as demonstrated by Dezsö et al. [58].

8. Conclusions

This study contains an analysis of the validity of the standard gradient-diffusion hypothesis for indoor dispersion modeling in an enclosure ventilated by a transitional wall jet ($Re \approx 2{,}500$). This is important because the standard gradient-diffusion hypothesis is often applied in ventilation studies, as well as in other research areas, to model the turbulent mass flux in steady RANS simulations of pollutant dispersion. The following conclusions can be made:

- The influence of the turbulent Schmidt number on the predicted mean concentrations in the enclosure is relatively small for this particular case. The results from simulations with $Sc_t = 0.3$ and $Sc_t = 1.0$ are within 25% and 12% of the simulation results obtained with the default value of $Sc_t = 0.7$, respectively.

- The convective mass fluxes obtained with LES and RANS in combination with the LR k-ε model are very similar. Larger differences are present between the results obtained with the two RANS turbulence models, which can be attributed to different mean flow fields, where the RSM shows a lower performance than the LR k-ε model.
- The convective mass fluxes in both the RANS and the LES simulations are at least one order of magnitude larger than the turbulence fluxes, indicating the stronger importance of transport by the mean flow in the overall dispersion process in the enclosure compared to that by the turbulent fluctuations.
- The results of the turbulent mass fluxes obtained with the LES model show that counter-gradient mechanisms are present inside the enclosure. As a result, the standard gradient-diffusion hypothesis is not valid in the entire flow domain. However, since the convective mass fluxes dominate over the turbulent mass fluxes in this particular case, the predicted concentration differences in the enclosure between LES and RANS with the LR k-ε ($Sc_t = 0.7$) are generally below 10% although local differences can go up to a factor 2.
- Future work should indicate whether the gradient-diffusion hypothesis is valid for other room geometries and flow configurations, and if not, to which extent this compromises the accuracy of the pollutant transfer in the enclosure.

9. Acknowledgements

Twan van Hooff has been a PhD student funded by both Eindhoven University of Technology in the Netherlands and the Research Fund – Flanders (Fonds Wetenschappelijk Onderzoek (FWO) - Flanders, Belgium) (FWO project number: G.0435.08). The FWO Flanders supports and stimulates fundamental research in Flanders. Its contribution is gratefully acknowledged.

The measurements reported in this paper were supported by the Laboratory of the Unit Building Physics and Services (BPS) at Eindhoven University of Technology and the Building Physics Section at the Katholieke Universiteit Leuven. Special thanks go to Jan Diepens, head of LBPS, and Wout van Bommel, Harrie Smulders and Geert-Jan Maas, members of the LBPS, for their valuable contribution.

10. References

[1] P.V. Nielsen, Berechnung der Luftbewegung in einem zwangsbelüfteten Raum. Gesundheits-Ingenieur, 94 (1973) 299-302.

[2] P.V. Nielsen, Flow in air conditioned rooms, PhD Thesis, Technical University of Denmark, Copenhagen, 1974.

[3] P.V. Nielsen, Prediction of airflow and comfort in air conditioned spaces, ASHRAE Trans. 81 (1975) Part II.

[4] H.B. Awbi, Application of computational fluid dynamics in room ventilation, Build. Environ. 24 (1989) 73-84.

[5] P.J. Jones, G.E. Whittle, Computational fluid dynamics for building air flow prediction. Current status and capabilities, Build. Environ. 27 (1992) 321-338.

[6] S. Kato, S. Murakami, A. Mochida, S. Akabayashi, Y. Tominaga, Velocity–pressure field of cross ventilation with open windows analyzed by wind tunnel and numerical simulation, J. Wind. Eng. Ind. Aerodyn. 44 (1992) 2575–2586.

[7] G. Gan, H.B. Awbi, Numerical simulation of the indoor environment, Build. Environ. 29(1994) 449-459.

[8] S. Murakami, S. Kato, R. Ooka, Comparison of numerical predictions of horizontal non-isothermal jet in a room with three turbulence models – k-ε EVM, ASM, and DSM, ASHRAE Trans. 100 (1994) 697–706.
[9] Q. Chen, Comparison of different k-ε models for indoor air-flow computations. Num. Heat Trans. Part B: Fund. 28 (1995) 353-369.
[10] Q. Chen, Prediction of room air motion by Reynolds-stress models, Build. Environ. 31 (1996) 233-244.
[11] Q. Chen, Ventilation performance prediction for buildings: A method overview and recent applications, Build. Environ. 44 (2009) 848-858.
[12] P.V. Nielsen, The selection of turbulence models for prediction of room airflow, ASHRAE Trans. 104(1B) (1998) 1119-1127.
[13] P.V. Nielsen, Computational fluid dynamics and room air movement, Indoor Air, 14 (2004) 134-143.
[14] J. Moureh, D. Flick, Wall air-jet characteristics and airflow patterns within a slot ventilated enclosure, Int. J. Therm. Sci. 42 (2003) 703-711.
[15] J. Moureh, D. Flick, Airflow characteristics within a slot-ventilated enclosure, Int. J. Heat Fluid Flow 26 (2005) 12-24.
[16] D.N. Sørensen, P.V. Nielsen, Quality control of computational fluid dynamics in indoor environments, Indoor Air 13 (2003) 2-17.
[17] T. van Hooff, B. Blocken, Coupled urban wind flow and indoor natural ventilation modeling on a high-resolution grid: A case study for the Amsterdam ArenA stadium, Environ. Modell Softw. 25 (2010) 51-65.
[18] T. van Hooff, B. Blocken, On the effect of wind direction and urban surroundings on natural ventilation of a large semi-enclosed stadium, Comput. Fluids 39 (2010) 1146-1155.
[19] Y. Li, P.V. Nielsen, CFD and ventilation research, Indoor Air 21 (2011) 442-453.
[20] T. van Hooff, B. Blocken, G.J.F. van Heijst, On the suitability of steady RANS CFD for forced mixing ventilation at transitional slot Reynolds numbers, Indoor Air 23 (2013) 236-249.
[21] C.A. Rundle, M.F. Lightstone, P. Oosthuizen, P. Karava, E. Mouriki, Validation of computational fluid dynamics simulations for atria geometries, Build. Environ. 46 (2011) 1343-1353.
[22] R. Ramponi, B. Blocken, CFD simulation of cross-ventilation for a generic isolated building: impact of computational parameters, Build. Environ. 53 (2012) 34-48.
[23] S.-J. Cao, J. Meyers, On the construction and use of linear low-dimensional ventilation models, Indoor Air 22 (2012) 427-441.
[24] K.C. Chang, W.D. Hsieh, C.S. Chen, A modified low-Reynolds-number turbulence model applicable to recirculating flow in pipe expansion, J. Fluids Eng. 117 (1995) 417-423.
[25] F.R. Menter, Two-equation eddy-viscosity turbulence models for engineering applications, AIAA J. 32 (1994) 1598–1605.
[26] D.C. Wilcox, Turbulence Modeling for CFD. DCW Industries, Inc., La Canada, California, 1998.
[27] B.E. Launder, G.J. Reece, W. Rodi, Progress in the development of a Reynolds-stress turbulent closure, J. Fluid Mech. 68(3) (1975) 537-566.
[28] Fluent Inc., Fluent 6.3 user's guide, Lebanon, US, 2006.
[29] C.L. Lubbers, G. Brethouwer, B.J. Boersma, Simulation of the mixing of a passive scalar in a round turbulent jet, Fluid Dyn. Res. 28 (2001) 189-208.
[30] G. He, Y.G. Andrew, T. Hsu, The effect of Schmidt number on turbulent scalar mixing in a jet-in-crossflow, Int. J. Heat Mass Transf. 42 (1999) 3727-3738.
[31] R. Chevray, N.K. Tutu, Intermittency and preferential transport of heat in a round jet, J. Fluid Mech. Part 1 88 (1978) 133-160.

[32] I. Yimer, I. Campbell, L.Y. Jiang, Estimation of the turbulent Schmidt number from experimental profiles of axial velocity and concentration for High-Reynolds-Number Jet Flows, Can. Aeronaut. Space J. 48 (2002) 195–200.
[33] D.B. Spalding, Concentration fluctuations in a round turbulent free jet, J. Chem.Eng. Sci. 26 (1971) 95-107.
[34] J.O. Hinze, Turbulence. Mcgraw-Hill, New York, NY, 1987.
[35] H.B. Awbi, Ventilation of buildings, London: Spon Press, 2003.
[36] W. Rodi, Turbulence Models and Their Application in Hydraulics – A State of the Art Review. International Association for Hydraulic Research, Delft, The Netherlands, 1984.
[37] Y. Tominaga, T. Stathopoulos, Turbulent Schmidt numbers for CFD analysis with various types of flowfield, Atmos. Environ. 41 (2007) 8091-8099.
[38] P. Gousseau, B. Blocken, G.J.F. van Heijst, CFD simulation of pollutant dispersion around isolated buildings: On the role of convective and turbulent mass fluxes in the prediction accuracy, J. Hazard. Mater. 194 (2011) 422-434.
[39] P. Gousseau, B. Blocken, G.J.F. van Heijst, Large-Eddy Simulation of pollutant dispersion around a cubical building: Analysis of the turbulent mass transport mechanism by unsteady concentration and velocity statistics, Environ. Pollut. 167 (2012) 47-57.
[40] P.V. Nielsen, Specification of a two-dimensional test case, Aalborg University, IEA Annex 20: Air Flow Patterns within Buildings, 1990.
[41] T. van Hooff, B. Blocken, T. Defraeye, J. Carmeliet, G.J.F. van Heijst, PIV measurements of a plane wall jet in a confined space at transitional slot Reynolds numbers, Exp. Fluids 53 (2012) 499-517.
[42] T. van Hooff, B. Blocken, T. Defraeye, J. Carmeliet, G.J.F. van Heijst, PIV measurements and analysis of transitional flow in a reduced-scale model: ventilation by a free plane jet with Coanda effect, Build. Environ. 56 (2012) 301-313.
[43] A.K. Prasad, Particle image velocimetry, Curr. Sci. 79 (2000) 51-60.
[44] R.D. Keane, R.J. Adrian, Optimization of particle image velocimeters. Part I: Double pulsed systems. Meas. Sci. Technol. 1 (1990)1202-1215.
[45] H.W. Coleman, W.G. Steel, Experimentation and uncertainty analysis for engineers. Wiley and Sons, New York, USA, 1999.
[46] K. Hanjalić, Advanced turbulence closure models: a view of current status and future prospects, Int. J. Heat Fluid Flow 15 (1994) 178–203.
[47] A. Schälin, P.V. Nielsen,Impact of turbulence anisotropy near walls in room airflow, Indoor Air 14 (2004) 159-168.
[48] J. Smagorinsky, General circulation experiments with the primitive equations. I. The basic experiment, Monthly Weather Rev. 91 (1963) 99-164.
[49] M. Germano, U. Piomelli, P. Moin, W.H. Cabot, A dynamic subgrid-scale eddy viscosity model, Phys. Fluids A 3 (1991) 1760-1765.
[50] D.K. Lilly, A proposed modification of the Germano subgrid-scale closure method, Phys. Fluids A 4 (1992) 633-635.
[51] P. Moin, K. Squires, W. Cabot, S. Lee, A dynamic subgrid-scale model for compressible turbulence and scalar transport, Phys. Fluids A3-11 (1991) 2746-2757.
[52] E. Sergent, Vers une méthode de couplage entre la simulation des grandes échelles et les modèles statistiques. Thèse présentée devant l'Ecole Centrale de Lyon, 2002.
[53] T. van Hooff, B. Blocken, L. Aanen, B. Bronsema, Numerical analysis of the performance of a venturi-shaped roof for natural ventilation: influence of building width, J. Wind. Eng. Ind. Aerodyn. 104-106 (2012) 419-427.

[54] P.V. Nielsen, Specification of a two-dimensional test case, Aalborg University, IEA Annex 20: Air Flow Patterns within Buildings, 1990.
[55] Y. Tominaga, T. Stathopoulos, Numerical simulation of dispersion around an isolated cubic building: model evaluation of RANS and LES, Build. Environ. 45 (2010) 2231-2239.
[56] K. Abe, K. Suga, Toward the development of a Reynolds-averaged algebraic turbulent scalar flux model, Int. J. Heat Fluid Flow 22 (2001) 19-29.
[57] B.J. Daly, F.H. Harlow, Transport equations in turbulence, Phys. Fluids 13 (1970) 2634–2649.
[58] G. Dezsö, A. Stitou, J.P.A.J. van Beeck, M.L. Riethmuller, Measurement of turbulent mass flux with PTV in a street canyon, J. Wind. Eng. Ind. Aerodyn. 91 (2003) 1117-1131.

FIGURES

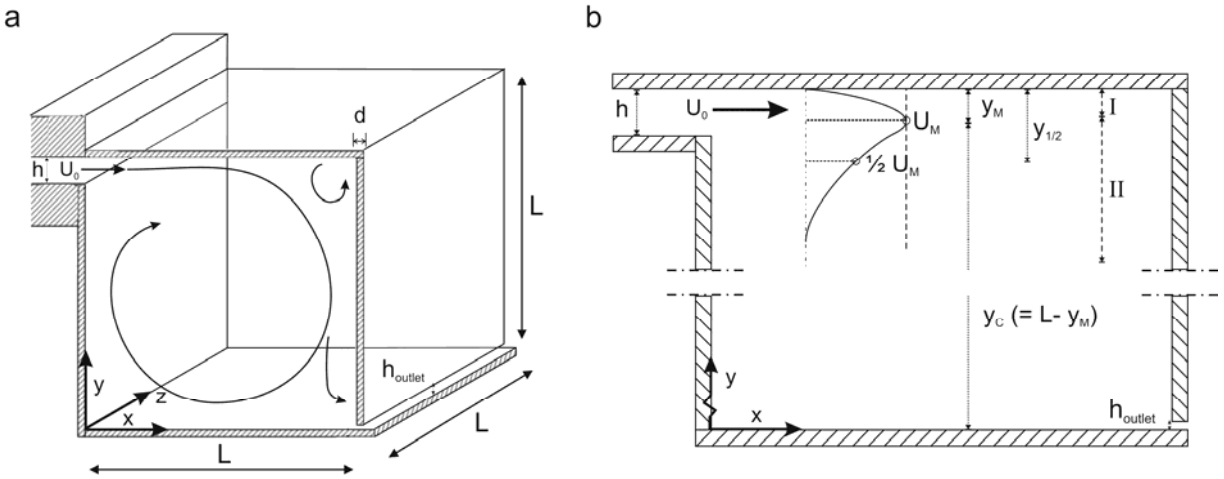

Fig. 1: (a) 3D room geometry with indication of coordinate system, inlet velocity U_0, inlet height h, outlet height h_{outlet}, thickness of the walls d, and dimensions of the test section L^3. (b) 2D schematic representation of the plane wall jet with I the inner region, II the outer region, U_M the maximum velocity, y_M the distance from the top wall to the location of U_M, y_C the distance from the bottom wall to the location of U_M and $y_{1/2}$ the location of ½ U_M in the outer region.

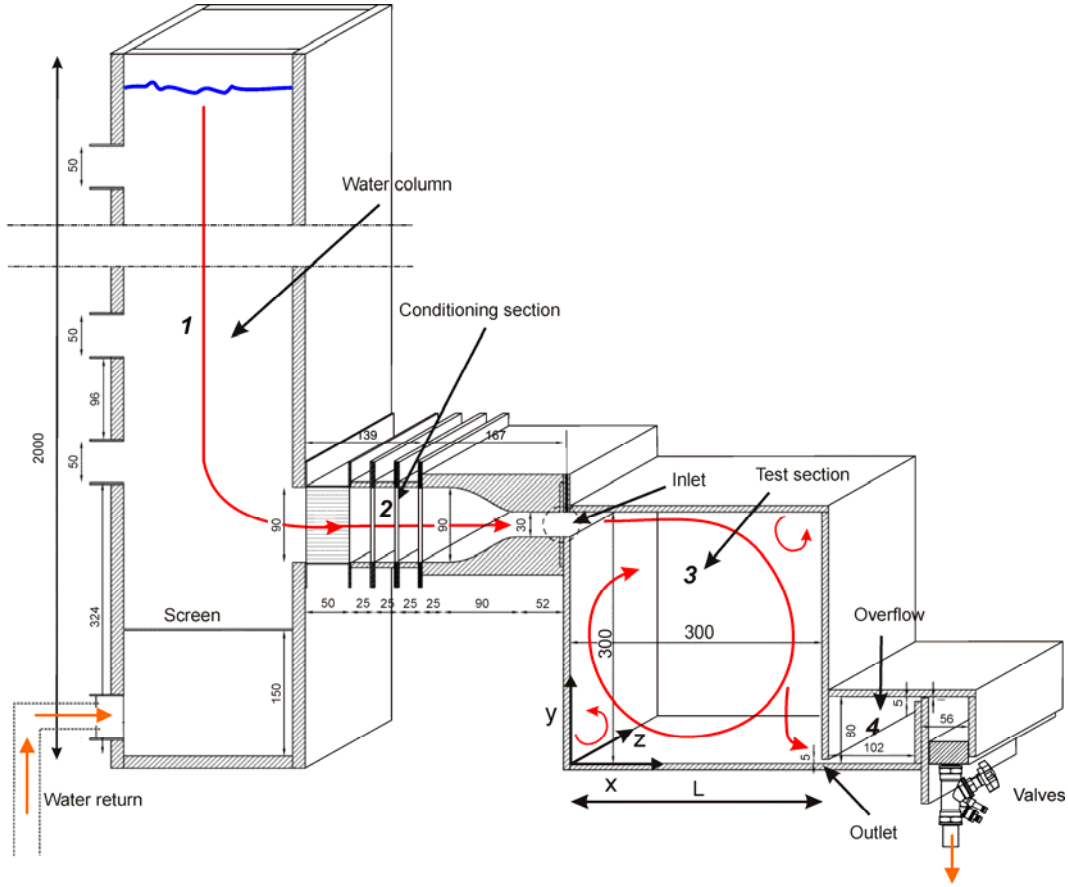

Fig. 2: Reduced-scale setup used for the flow visualizations and PIV measurements: (1) water column; (2) flow conditioning section in front of the inlet, (3) test section, (4) overflow, and the valves that are placed in a block after the overflow. Dimensions in mm.

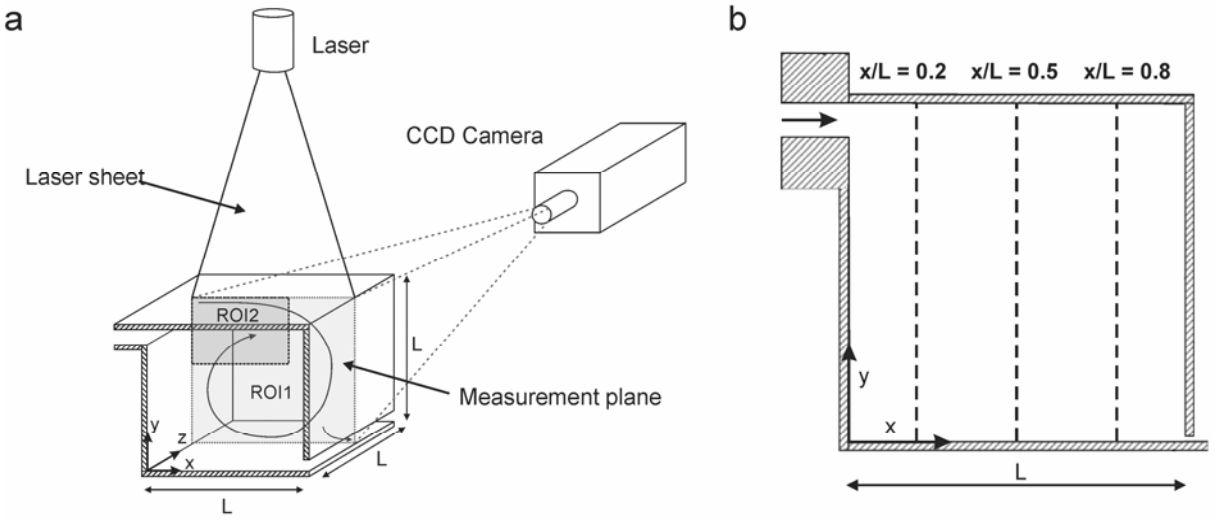

Fig. 3: (a) PIV measurement setup; the laser head is positioned above the test section using a translation stage. ROI1 indicates the region of interest (L x L) for the first measurement set, ROI2 indicates the region of interest of 0.6L x 0.4L (W x H) for the second set. (b) Indication of vertical lines along which experimentally and numerically obtained velocities will be compared in section 6.

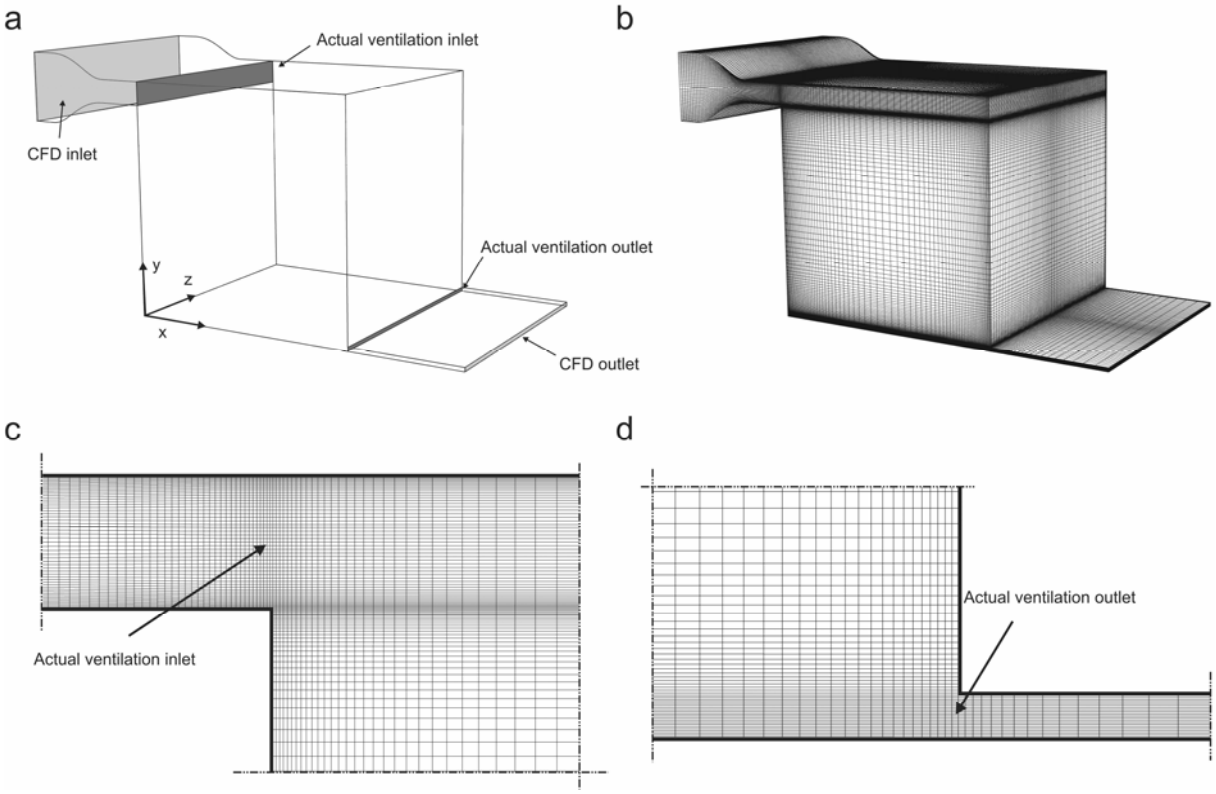

Fig. 4: (a) Computational model of the water cube. (b) Computational grid (1,386,400 cells). (c) Detail of computational grid at the actual ventilation inlet with 50 cells over the inlet height. (d) Detail of computational grid at the actual ventilation outlet with 20 cells over the outlet height.

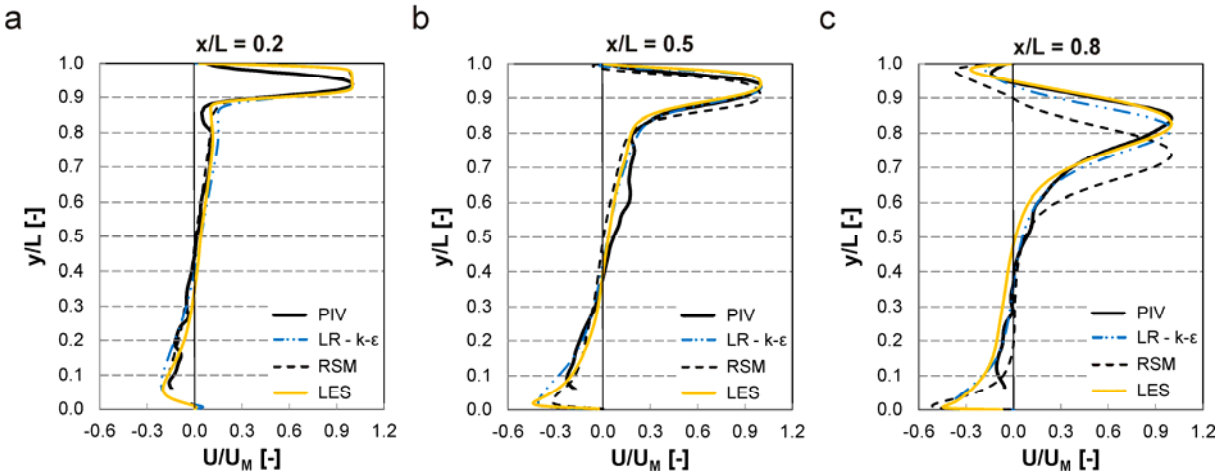

Fig. 5: Comparison of mean velocity profiles by PIV in ROI1 with results of steady RANS CFD simulations and LES simulation for Re ≈ 2,500. (a) U/U_M at x/L = 0.2; (b) x/L = 0.5; (c) x/L = 0.8.

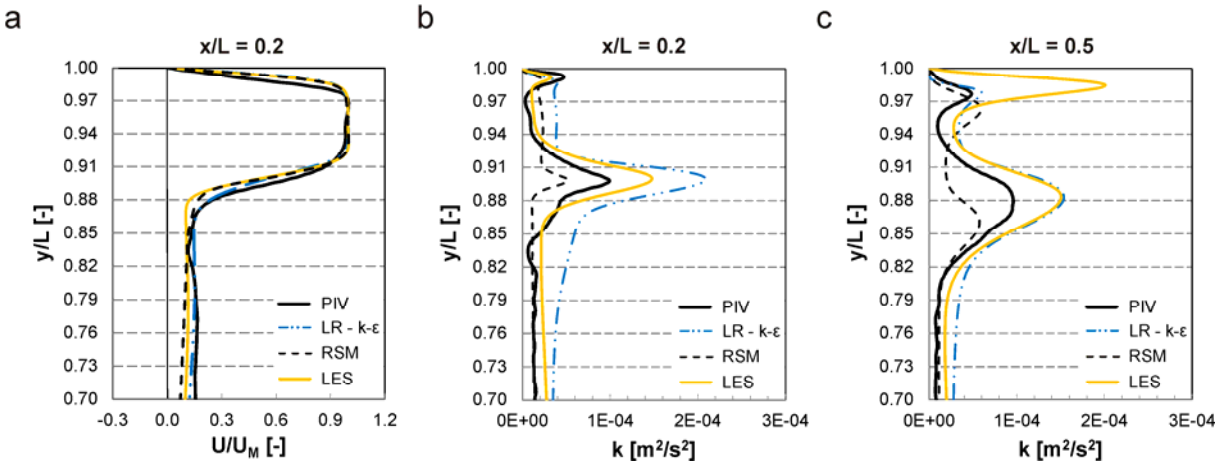

Fig. 6: (a) Comparison of mean velocity profiles U/U_M at x/L = 0.2 by PIV in ROI2 with results of steady RANS CFD simulations and LES simulation. (b-c) Comparison of measured turbulent kinetic energy k and values obtained from CFD simulations: (b) x/L = 0.2 and (c) x/L = 0.5.

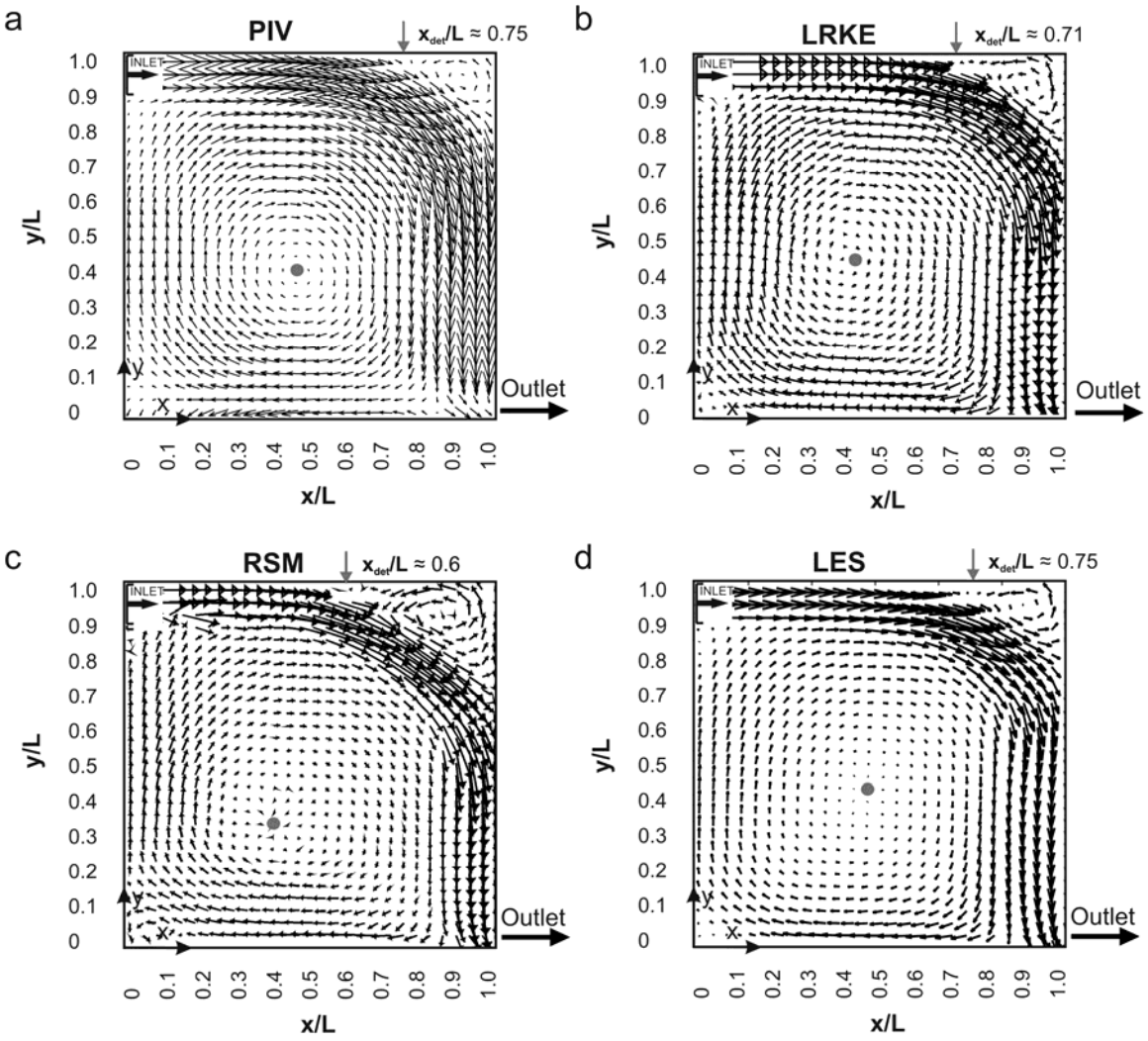

Fig. 7: Time-averaged velocity vector fields in the vertical center plane (z/L = 0.5), with indication of the location of jet detachment (x_{det}/L) and the center of the recirculation cell (●). (a) PIV measurements; ● = (0.47; 0.41); (b) LR k-ε; ● = (0.44; 0.43); (c) RSM: ● = (0.40; 0.34); (d) LES; ● = (0.47; 0.43).

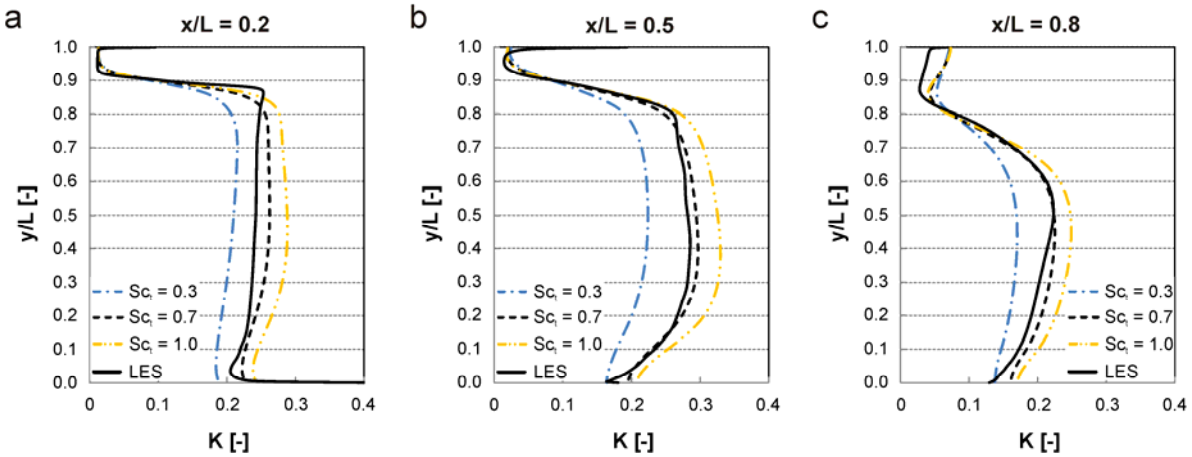

Fig. 8: Vertical profiles of dimensionless concentration K obtained with the LR k-ε model and a Sc_t value of 0.3, 0.7 and 1.0, and with LES. (a) x/L = 0.2; (b) x/L = 0.5; (c) x/L = 0.8.

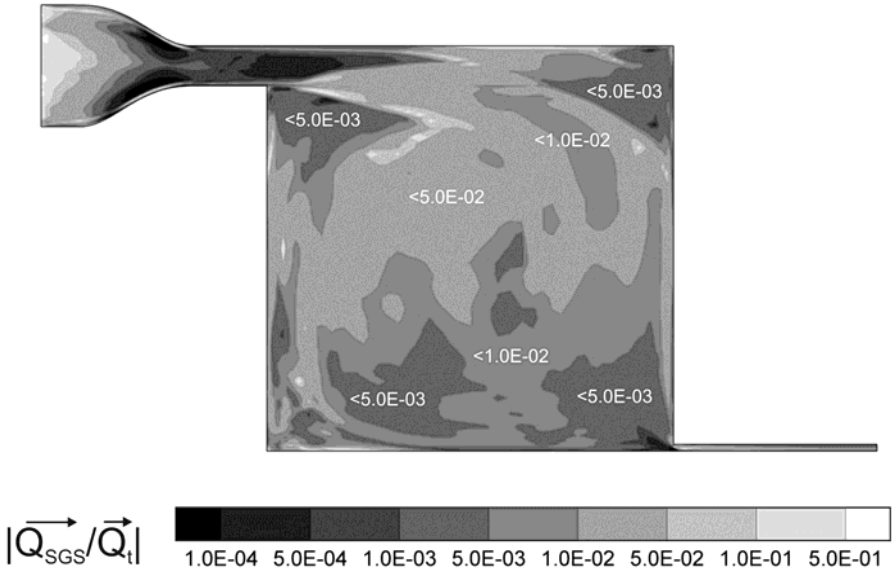

Fig. 9: Relative contribution of the magnitude of the SGS mass flux to the magnitude of the total turbulent mass flux in the vertical center plane ($\left|\overrightarrow{Q_{SGS}}/\overrightarrow{Q_t}\right|$).

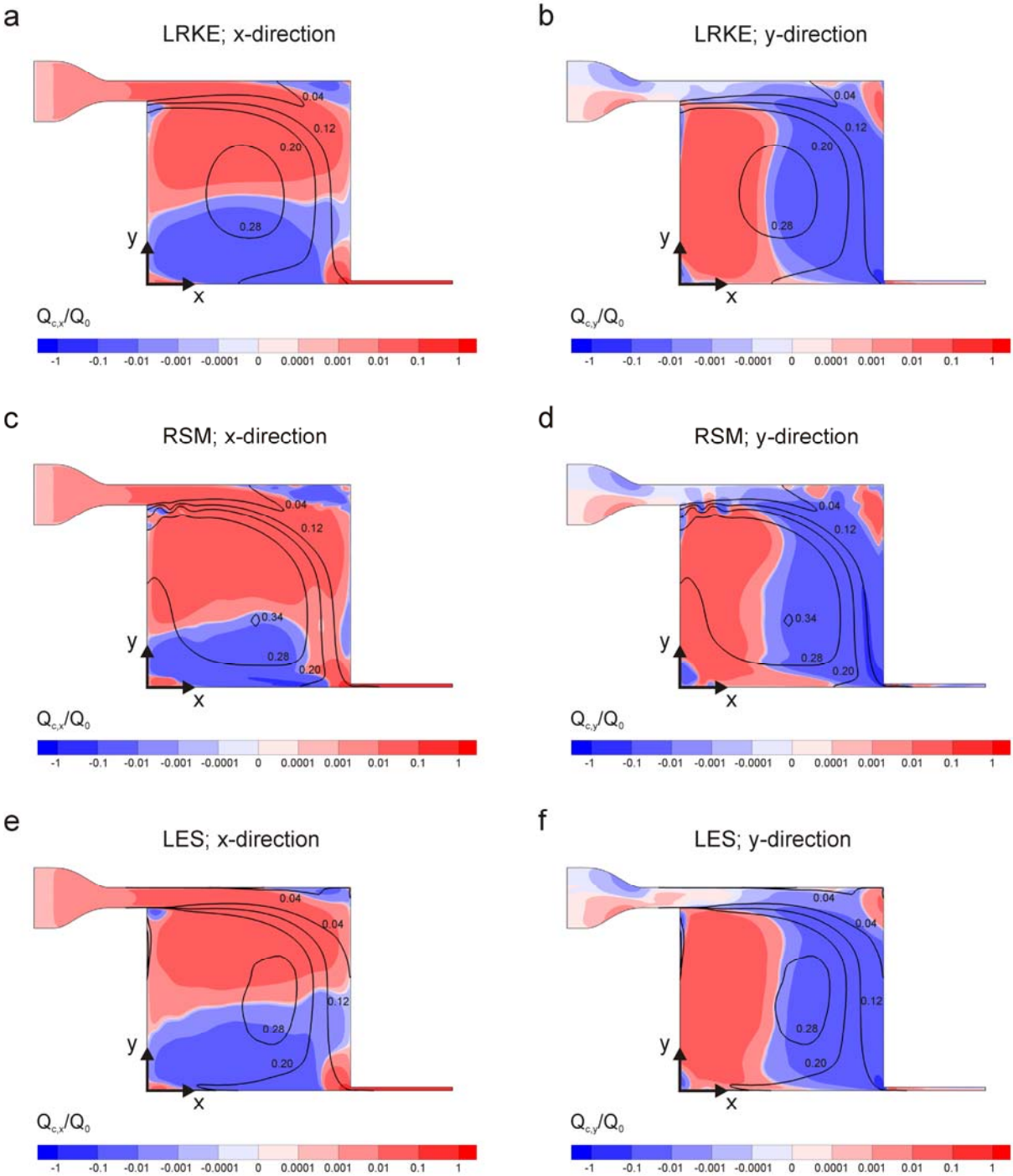

Fig. 10: Contours of the streamwise ($Q_{c,x}/Q_0$) (a,c,e) and vertical ($Q_{c,y}/Q_0$) (b,d,f) non-dimensional convective mass fluxes in the vertical center plane (z/L = 0.5) of the enclosure obtained with steady RANS and LES. (a,b) Low-Reynolds k-ε. (c,d) RSM. (e,f) LES. The solid lines are isolines of K = 0.04; 0.12, 0.20, 0.28 and 0.34.

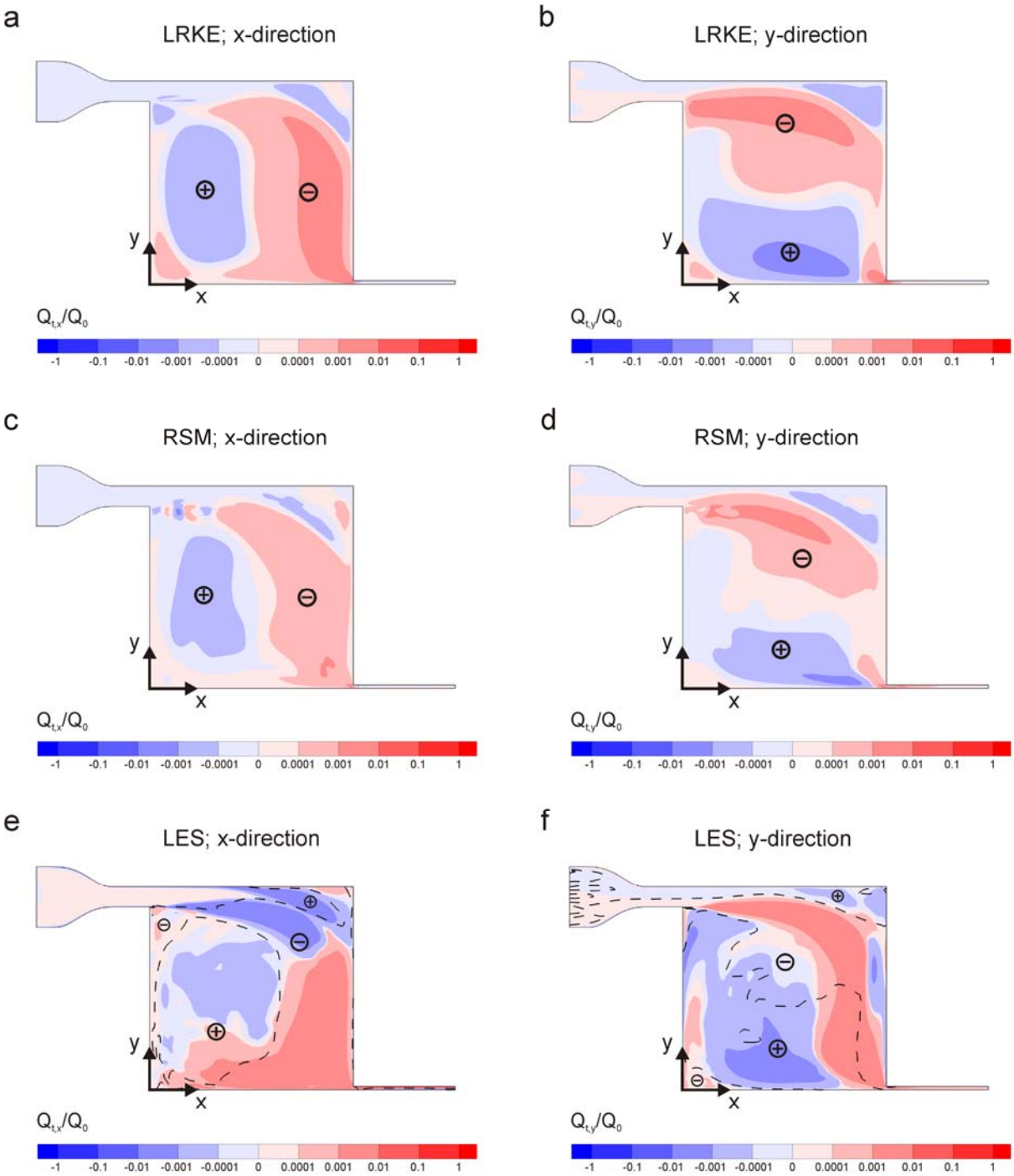

Fig. 11: Contours of the streamwise ($Q_{t,x}/Q_0$) (a,c,e) and vertical ($Q_{t,y}/Q_0$) (b,d,f) non-dimensional turbulent mass fluxes in the vertical center plane (z/L = 0.5) of the enclosure obtained with steady RANS and LES. (a,b) Low-Reynolds k-ε. (c,d) RSM, (e,f) LES. The dashed lines in (e,f) represent the isolines $\partial C/\partial x_i = 0$ in the corresponding direction: (e) $x_i = x$, (f) $x_i = y$. On each side of the isoline, the sign of $\partial C/\partial x_i$ is indicated in circles (+: positive; -: negative). The CG mechanism of turbulent mass transport is characterized by $Q_{t,i}/Q_0$ and $\partial C/\partial x_i$ of the same sign.

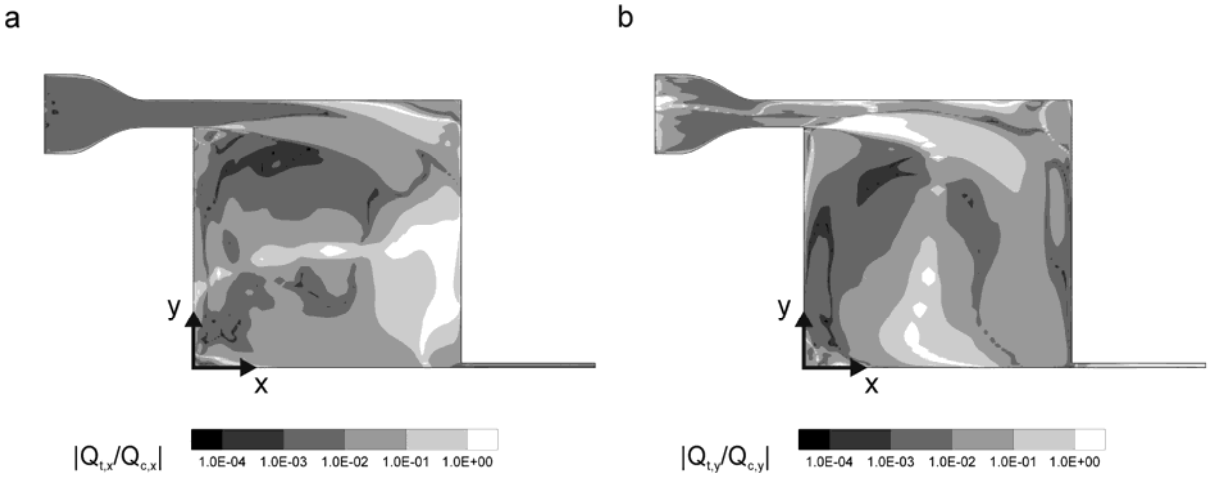

Fig. 12: Ratio of turbulent mass flux to convective mass flux in vertical center plane. Contours of (a) $|Q_{t,x}/Q_{c,x}|$; (b) $|Q_{t,y}/Q_{c,y}|$.

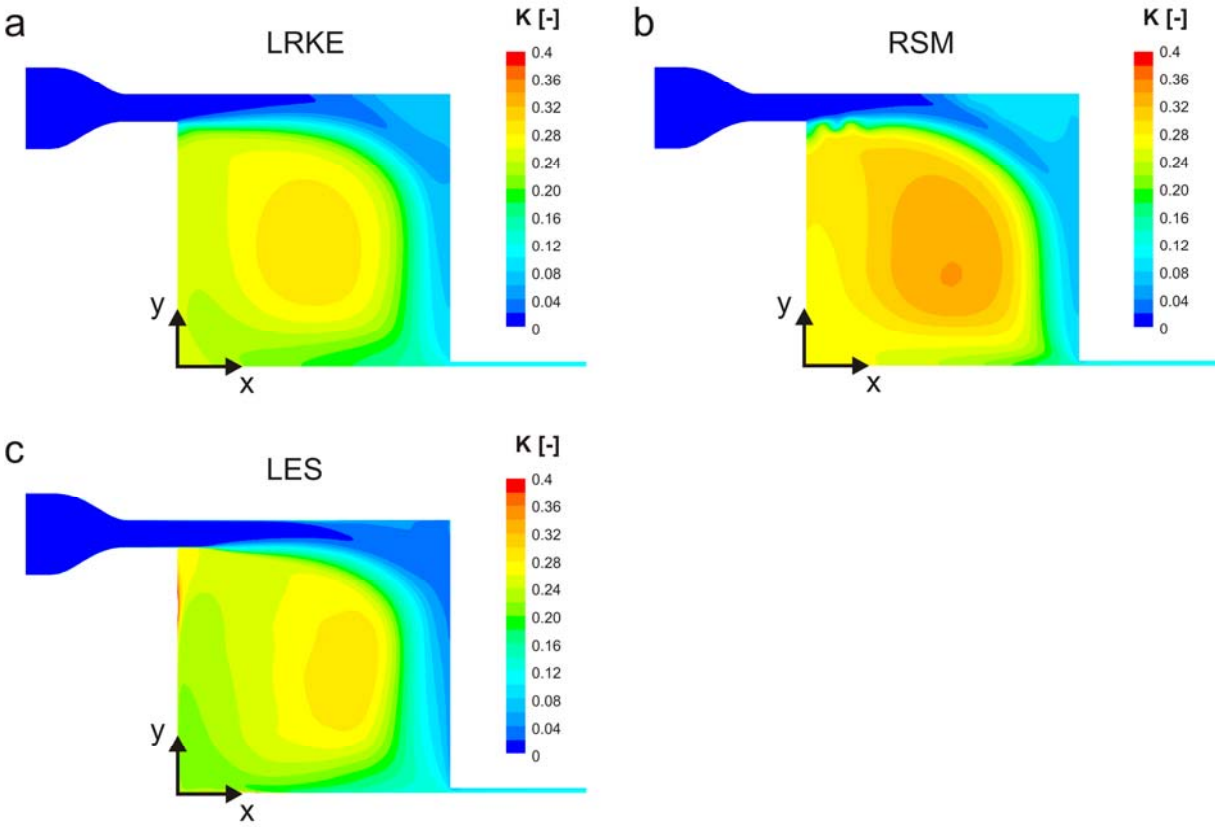

Fig. 13: Contours of dimensionless concentration K in the vertical center plane. (a) LR k-ε; (b) RSM; (c) LES.